Kα Cold-Target Imaging and Preheat Measurement Using a Pinhole-Array X-Ray Spectrometer

Two-dimensional (2-D) monochromatic imaging of laser-imploded targets[1–6] is useful for diagnosing target compression and stability. Here we present a simple method for such imaging, using an array of about 300 pinholes placed in front of a flat-crystal x-ray spectrometer. The main advantage of this method (in addition to its simplicity) is the ability to simultaneously obtain a large number of images over a wide range of photon energies. This is particularly useful for imaging the emission region of a single spectral line from a doped target, where images around the wavelength of the line can be simultaneously obtained and subtracted from the image at the line. Imaging a spectral line of a dopant can be useful for studying mixing of target layers. *Here we use the array to image Kα fluorescence from a titanium-doped target (excited by core radiation) and thereby obtain an image of the cold layer at peak compression*. This image can otherwise be obtained only through backlighting. Using a flat crystal limits the field of view, but this limitation is shown not to be severe when imaging the compressed target core. On the other hand, the narrow field of view translates into improved spectral resolution. We show that sufficient intensity can be obtained in monochromatic imaging even without the gain in intensity when using a focusing crystal. In addition, the array provides spectra of high spectral resolution because of the reduction in the effective source size. Finally, we show that, in addition to the core-pumped Kα emission, a second Kα-emitting zone of a larger radius appears in the image. This Kα emission is pumped during the laser-irradiation pulse, indicating preheat by suprathermal electrons.

Figure 75.23 shows the geometry of the pinhole array placed in front of a crystal spectrometer. The dispersion direction indicated in Fig. 75.23 is determined by the orientation of the array with respect to the crystal. Rays from the target traversing different pinholes fall on the crystal at different angles; thus, different wavelengths are diffracted. The distance between adjacent pinholes (750 μm) is chosen so that adjacent images on the film are close but not overlapping. Rays from different parts of the target traversing the same pinhole also fall on the crystal at different angles; thus, the target image from continuum radiation is not monochromatic; rather, the photon energy across the image (in the dispersion direction) varies over a finite interval. A single spectral line will show the image of only a narrow section of the target (in the dispersion direction); however, the compressed core can be imaged by a spectral line of sufficient spectral width. In the direction of dispersion, the shift in the average photon energy between adjacent images is typically ~100 eV. The line of pinholes in a direction perpendicular to that of the crystal dispersion is slightly tilted, causing a small photon-energy shift (of the order of ~10 eV) between two adjacent images in that direction; thus, an array of 30×10 pinholes can produce 300 images with energies spread over the range of, say, 4 to 7 keV. The advantage due to the tilt in the vertical lines of pinholes can be viewed in two ways: (a) for a given target location, adjacent images correspond to slightly shifted photon energy, or (b) for a given spectral line, adjacent images correspond to slightly different sections of the target. The properties of array imaging,

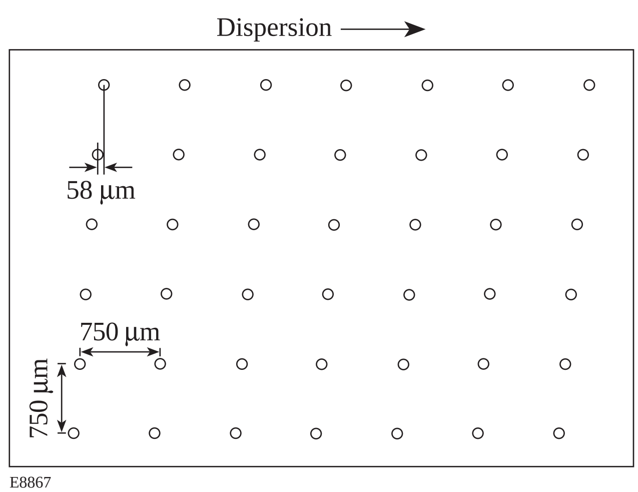

Figure 75.23
The geometry of the pinhole array placed in front of the spectrometer. Each of about 300 pinholes yields a narrow-band, 2-D image at a slightly shifted photon energy. The 58-μm shift due to the tilt in the vertical direction yields an energy shift between adjacent images of ~6 to 10 eV in the range of 4 to 5 keV.

in conjunction with the test results shown in Figs. 75.24 and 75.27, will be further discussed below.

Two arrays of the type shown in Fig. 75.23 were used to image targets imploded on the 60-beam OMEGA laser system.[7] In both cases, the target consisted of a polymer shell containing an embedded, titanium-doped layer. We show two examples of such tests: In the first shot (a) an array of 50-μm-diam pinholes (in 25-μm-thick Pt foil) was used, and the results are shown in Fig. 75.24 (this figure is used mostly to illustrate the properties of array imaging). In the second shot (b) an array of 25-μm-diam pinholes (in 12.5-μm-thick Pt foil) was used and the results are shown later in Fig. 75.27 (this figure is used mostly to illustrate the imaging of the cold, compressed shell through Kα-line fluorescence). Except for the pinhole size and foil thickness, the two arrays had the same geometry as in Fig. 75.23.

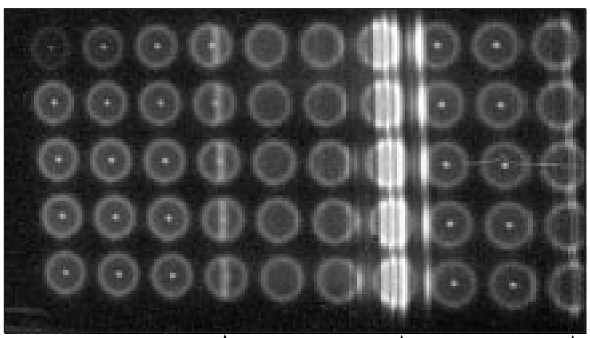

Figure 75.24
Part of the ~300 array-spectrometer images obtained with an array of 50-μm pinholes, from a titanium-coated target implosion [shot (a)]. Because of the vertical tilt in the array (see Fig. 75.23), the target section imaged by a given spectral line shifts for successive images in that direction. Lines (such as the Heα line) from a different target location can reappear on a neighboring image.

Properties of Array Imaging

In shot (a) a CH polymer shell of 867-μm inner diameter and 13.7-μm thickness was doped with titanium at 7% by atom number, overcoated by 13.9-μm-thick undoped CH. The fill gas was 10 atm deuterium. The laser pulse was a 1-ns flat pulse (to within ±5%) with 0.1-ns rise and fall times and 29.8 kJ of energy. Figure 75.24 shows part of the array images obtained with a Ge(111) diffracting crystal. The dispersion direction is horizontal—a tilt in the images in the vertical direction is evident. Both the Ti-Kα line and lines of Ti^{20+} (helium-like) and Ti^{21+} (hydrogen-like) ions are marked. The Ti^{20+} Heα line and its dielectronic satellites reappear on neighboring images. This is due to parallel rays emanating from different target locations and traversing adjacent pinholes. Without the array, these two groups of lines would be part of a broad spectral feature representing emission from the whole target. The array transmits rays from only two target slices.

Individual lines yield monochromatic images of only a section of the target (because rays from other target sections do not satisfy the Bragg diffraction condition for that line). On the other hand, the continuum radiation gives rise to complete target images; however, these images are not monochromatic—the photon energy shifts across the image in the direction of dispersion (by ~100 eV). The energy shift between adjacent images in the dispersion direction varies from ~80 eV (at 4 keV) to ~130 eV (at 5 keV). The tilt in the vertical direction causes a photon-energy shift between two adjacent images that varies from ~6 eV (at 4 keV) to ~10 eV (at 5 keV).

The narrow field of view for individual lines (in the direction of dispersion) can be remedied by replacing the flat crystal with a curved crystal in the Rowland-circle geometry;[2,3,5] however, Fig. 75.24 shows that typical lines can be spectrally wide enough for imaging the core even with a flat crystal. This is seen simply in the fact that the lines are about as broad as the target core (e.g., in the lowest image in the column marked "Kα"). The width of the lines in this context refers to their spectral width, transformed into a spatial width in the image. This transformation is obtained by differentiating the Bragg law for diffraction, from which the spatial extent Δx covered by a single spectral line of width ΔE (in the direction of dispersion) can be obtained. The result is $\Delta x = (\Delta E/E)L \tan\theta_B$, in terms of the Bragg angle θ_B and the target distance to the film (along the relevant ray). The spatial width of the Kα line in the direction of dispersion is ~130 μm. Part of it is due to the pinhole size (50 μm), but most of it is due to the spectral width of the Kα line (a larger pinhole size increases the field of view in the direction of dispersion but reduces the spatial resolution in both directions). Deconvolving the pinhole broadening from the total width shows that the spectral width of the line is ~5 eV and that the spatial width would be ~120 μm when using a very small pinhole. Thus, a flat crystal can yield 2-D Kα monochromatic images of only the core; however, there is no limitation on the field of view in the direction perpendicular to that of the dispersion. Furthermore, because the pinholes tilt in the vertical direction, the position of a given spectral line shifts across the target image for successive images in that direction, as is clearly evident in Fig. 75.24; thus, the combination of successive images in the vertical direction delineates the total emission region of the line. This works particularly well for the Kα line since its linewidth (~5 eV) is about the same as the average energy shift between successive images in the vertical direction (~6 eV). In higher-performing implosions the shell temperature would be higher so that some *M*-shell electrons would be ionized; in that case, the Kα line would be broader due to the overlapping of shifted lines from various charge states, and the field of view would then broaden. Also, in such implosions the compressed core is smaller and would thus require a smaller field of view.

The Ti^{20+} and Ti^{21+} lines in Fig. 75.24 are seen to be emitted from the target periphery, i.e., the hot laser-absorption region. On the other hand, the Kα line is emitted by the cold part of the Ti-doped layer following the photoionization of *K*-shell electrons. The source of this radiation can be either the coronal emission during the laser irradiation or the core radiation during peak compression. The Kα line emission in Fig. 75.24 is seen to come from a layer inside the hot corona region: the diameter of the coronal rings is ~900 μm, whereas the length of the Kα emission region perpendicular to the dispersion direction is only ~750 μm, and it peaks near its extremities. Thus, the radiation from the laser-heated corona pumps the fluorescence of Kα in the cold shell underneath the coronal region. An additional peak can be seen at the target center, indicating the possible Kα emission pumped by core radiation. This point is discussed in more detail in the next section, where the results of shot (b) clearly indicate Kα fluorescence pumped primarily by core radiation.

An important advantage of this device is the ability to reliably subtract the continuum images off a spectral line from the image on the line, thus obtaining the image of the region emitting that line. This is further discussed in conjunction with Fig. 75.27, where the cold shell is imaged through its Kα fluorescence. Additionally, the core spectrum can be easily separated from the coronal emission and plotted over a wide spectral range with good spectral resolution. Additional useful information in Fig. 75.24 is the absence of target cores in the spectral range of ~4.5 to 4.7 keV and above ~4.9 keV due to absorption of core radiation in the cold titanium layer. This absorption is due to titanium 1*s*–2*p* absorption lines and absorption above the Ti *K* edge, respectively.[8]

The array spectrometer can be alternatively used for achieving high spectral resolution: in the case of a large emitting source (such as emission prior to peak compression) the pinholes limit the effective source size and thus improve spectral resolution. For example, the fine-structure splitting of the Hα line of titanium is clearly seen in Fig. 75.24, indicating a resolution higher than 500. Without the pinhole array the whole target would radiate the line and the spectral resolution would be less than 100. In Fig. 75.25 the lineout in the direction of dispersion shows that a high-resolution spectrum can be obtained from a large source for lines that are much stronger than the continuum. In that case, the images formed by the continuum can be subtracted and the net line emission obtained. In general, the lineout can be recorded as a function of target position (perpendicular to the direction of dispersion). To facilitate the continuum-image subtraction, the lineout in Fig. 75.25 was chosen to avoid the core emissions. To further illustrate the high spectral resolution, we compare (in Fig. 75.26) part of the spectrum of Fig. 75.25 with that obtained simultaneously by an identical spectrometer where the pinhole array has been replaced by a 50-μm-wide slit. In the latter spectrum, the lines are considerably broadened due to the source size (~0.8 mm). They are further affected by the spatial distribution of target emission; because of the limb effect, the spectral lines appear on film as partly overlapping rings, giving rise to spurious splits in the spectrum. An 0.8-mm source size corresponds in the present arrangement without the array to a spectral resolution $E/\Delta E$ of ~130, whereas the pinhole-array spectrum in Fig. 75.26 shows a spectral resolution $E/\Delta E$ higher than ~500.

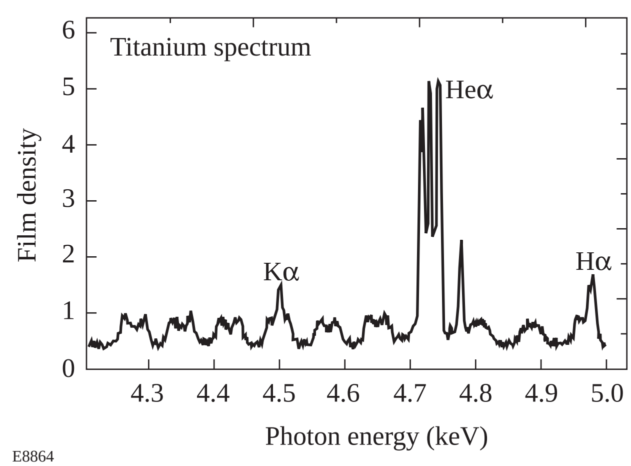

Figure 75.25
Lineout of Fig. 75.24 in the direction of dispersion (avoiding the cores), showing that a high-resolution spectrum from a large source can be obtained by using a pinhole-array spectrometer. For lines that are much stronger than the continuum, the images (that are due to the continuum) can be subtracted away. The line at ~4.8 keV is the Ti Heα line (from a different target location) transmitted though an adjacent pinhole.

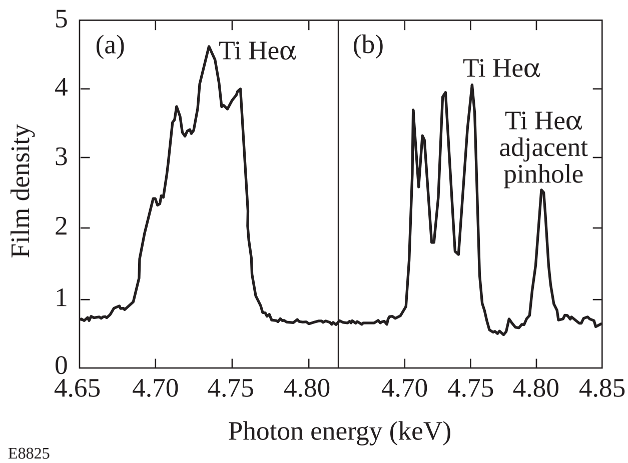

Figure 75.26
Comparison of the Ti Heα line manifold obtained simultaneously with and without the pinhole array. The Heα line ($2p^1P$–$1s$ transition in Ti^{20+}) is well resolved from its low-energy satellites when using the array. Without the array the lines are considerably broadened by the ~0.8-mm source size.

Imaging the Cold Shell with Kα Fluorescence

In shot (b), an empty CD polymer shell of 898-μm inner diameter and 5.9-μm thickness was coated with an 11.7-μm-thick layer of CH doped with titanium at 2% by atom number, overcoated by 13.5-μm-thick undoped CH. The laser pulse shape was the same as in shot (a), and its energy was 27.1 kJ.

Figure 75.27 shows part of the array images from target shot (b) obtained with a PET(002) diffracting crystal. The laser-irradiation uniformity in this shot was deficient, leading to a nonuniform implosion. We chose to display a section of the array images where the Kα line image is centered on the target core (second image from left). For images above and below this image the Kα line moves off target center toward the left and right, respectively. The Ti^{20+} lines (indicative of hot plasma) are seen to be emitted from the periphery of the target. On the other hand, a ring of emission at the wavelength of the Ti Kα line (indicative of a cold plasma) is seen to be emitted around the compressed core. This is evident when comparing the emission around the core in the second image from left to that in the other images. The nonsphericity of the Kα emission pattern is discussed below. The spatial features of these lines indicate that the Ti Heα line is emitted during the laser-irradiation time, whereas the Kα line is emitted around peak compression and is pumped by core radiation. These conclusions are consistent with the streaked spectra obtained for shot (b). Figure 75.28 shows lineouts of streaked spectra at three different times of the implosion: t_1– during the laser-irradiation period (lasting about ~1 ns); t_2–during the shell coasting when no radiation is emitted (lasting about 0.8 ns); and t_3–during peak compression, or stagnation (lasting about 0.2 ns). It is clearly seen that the Ti^{20+} Heα line is emitted during the laser irradiation; more precisely, the streak record shows that it is emitted toward the end of the laser pulse, when the burnthrough of the polymer overcoat has reached the doped layer. On the other hand, the Kα line is emitted during peak compression. This is entirely consistent with the conclusions drawn from the spatial patterns of these lines. In addition to the Kα line, the spectrum at peak compression also shows strong absorption above the Ti K edge. This is absorption of core radiation by the cold shell around the core and is precisely the source of photoionization leading to Kα fluorescence;[9] this observation provides an additional indication that the Kα line is pumped by core radiation at peak compression. The drop of intensity above the K edge can be used to estimate the areal density ($\rho\Delta r$) of the doped layer at peak compression and from here the total $\rho\Delta r$ of the compressed shell. It should be pointed out that there is very little change in the K-shell absorption at a given energy when M- or L-shell electrons are ionized.[10] In this case, however, the transmitted intensity above the K edge is too weak to determine the areal density, and only a lower limit of the $\rho\Delta r$ can be obtained. Assuming transmission of less than ~10% at the K edge, the areal density of the doped layer is $\rho\Delta r$ > 22 mg/cm^2. The total areal density of the compressed shell (that includes the undoped mandrel) can be estimated[8] as $\rho\Delta r$ > 32(±6) mg/cm^2.

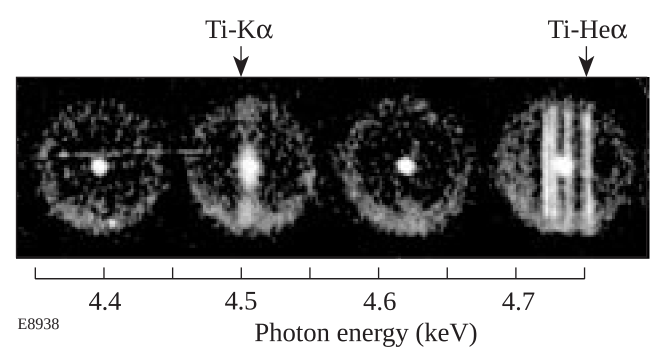

Figure 75.27
Part of the array images from target shot (b). The Ti^{20+} lines are seen to be emitted from the periphery of the target. On the other hand, a ring of emission at the wavelength of Ti Kα line is seen to be emitted around the compressed core. The Kα line is excited by core radiation, and its image delineates the cold shell at peak compression (see Fig. 75.28).

Figure 75.27 indicates that the Kα linewidth is insufficient for imaging the full extent of the cold shell in the dispersion direction. Since no limitation of field of view applies to the perpendicular direction, the Kα image is elliptically shaped. The vertical profile of the Kα emission shows the true dimension of the cold shell. By combining successive images in the vertical direction, we can obtain at least a qualitative view of the 2-D image of the cold shell. As mentioned above, in future high-performance implosions a single image may be sufficient for obtaining the 2-D image of the cold shell.

Using vertical lineouts in Fig. 75.27 we can obtain the dimensions of the cold shell in that direction. Figure 75.29(a) shows two such lineouts: (a) through the center of the second image from the left ("on Kα") and (b) an average of lineouts through the centers of the neighboring images on each side ("off Kα"). The peaks of the two profiles varied by about 10% (possibly due to fluctuations in pinhole sizes) and were normalized to the same height. The difference between these two curves [shown in Fig. 75.29(b)] delineates a ring-shaped layer of cold Ti-doped shell. Changing the relative intensity of the two profiles in Fig. 75.29(a) within the 10% uncertainty changes mostly the central minimum in Fig. 75.29(b), but not the overall shape and dimensions of the intensity ring. Alternative off-Kα profiles could be chosen by moving above and below the Kα image in Fig. 75.27 (sufficiently for the Kα emission to disappear); however, the closeness of peak intensity of the two profiles in Fig. 75.29(a) indicates that the choice adopted here is adequate. The nonuniformity of the implosion seen in the images of Fig. 75.27 is also evident in Fig. 75.29(b). Figure 75.29(a) also shows Kα emission at a ~300-μm radius. This delineates the position of the cold shell during the laser pulse, when it is pumped by radiation and suprathermal electrons from the laser-heated material; this is further discussed in the following section. Figure 75.29(a) shows higher Kα intensity around +300 μm than around –300 μm, again indicating nonuniformity. This nonuniformity mirrors the nonuniformity during peak compression: the peak of the Kα profile around +80 μm is higher than the peak around –80 μm. This is surely the result of the irradiation nonuniformity as evident in Fig. 75.27: The coronal emission in the four

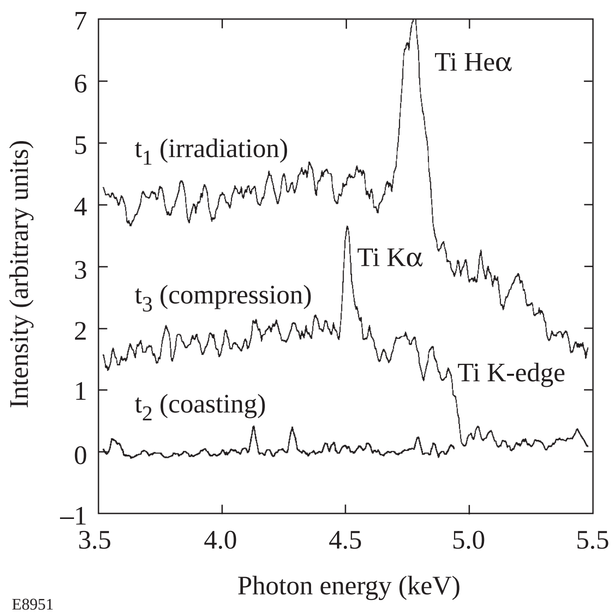

Figure 75.28
Spectra recorded by a streaked spectrograph at three times during the implosion of shot (b). The Ti^{20+} line emission occurs during the laser-pulse irradiation, t_1, whereas the *K*-edge absorption and the concomitant Kα line emission occur about ~1 ns after the end of the laser pulse, at the time of peak compression, t_3; t_2 is a time during the intervening coasting. These results confirm the conclusions from Fig. 75.27. Positive axis direction corresponds to downward direction in Fig. 75.27.

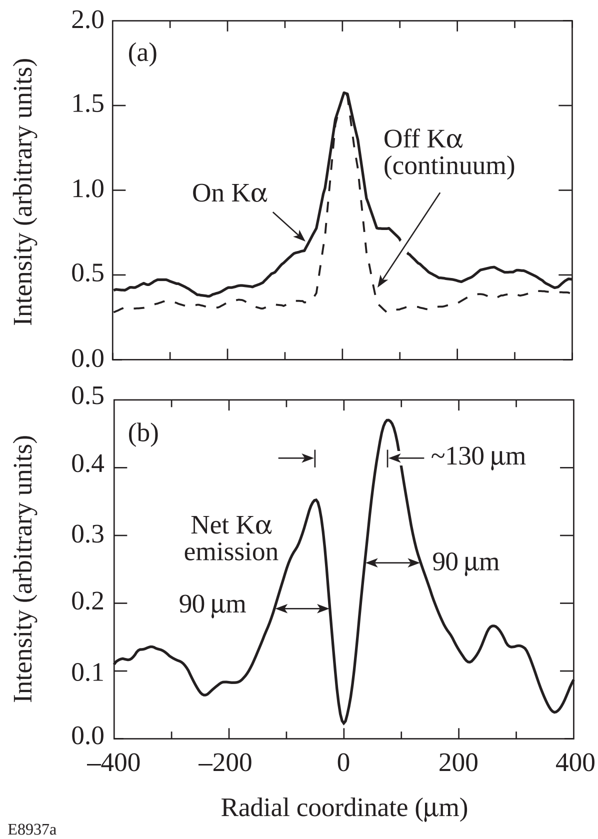

Figure 75.29
(a) Lineouts through images of Fig. 75.27, in the vertical direction (perpendicular to the direction of dispersion). The "on Kα" curve is through the center of the second image from the left; the "off Kα" curve is an average of lineouts through the centers of the two neighboring images on each side. (b) The difference between the two curves in (a) delineates the cold Ti-doped shell.

images is more intense on the lower half of the target, corresponding to a higher intensity of Kα (the positive axis in Figs. 75.29 and 75.30 corresponds to the downward direction in Fig. 75.27). Figure 75.29(b) indicates, for the cold shell, a ring of ~90-μm thickness and an average diameter of ~130 μm. In a previous experiment,[9] the Kα from a similar Ti-doped target was imaged in one dimension using a slit in front of a flat-crystal spectrometer. With one-dimensional (1-D) imaging, a ring-shaped source results in a flat-topped profile, and only the outer diameter of the ring can be reliably determined. The FWHM of the Kα profile in Ref. 9 (~250 μm) is similar to the FWHM in Fig. 75.29(b); however, the array yields an actual image of the ring of Kα emission (the profiles in Fig. 75.29 are slices through a 2-D image rather than 1-D images). The Kα emission profile and the *K*-edge absorption relate to the same target region, namely, the cold doped layer; thus, the ring thickness from Fig. 75.29(b) and the areal density derived from the *K*-edge absorption can be used to estimate the shell density. As noted above, the ablated part of the doped layer emits the Heα line of titanium, whereas the unablated doped layer emits the Kα line. The thickness of the doped layer (~90 μm) found in Fig. 75.29(b) is larger than the actual thickness at peak compression because of the time integration. Also, the areal density estimated above was only a lower limit; thus, a lower limit for the density of the doped layer can be obtained by dividing the estimated $\rho\Delta r$ of that layer (22 mg/cm^2) by its thickness (~90 μm) to yield ρ > 2 g/cm^3. This low density (albeit only a lower limit) is to be expected in view of the deficient symmetry of the laser irradiation in this experiment. A better determination of the shell density can be obtained by (a) lowering the level of doping to avoid complete *K*-edge absorption and (b) time-gating the spectrometer to avoid smearing due to time integration.

Preheat Measurement Using Early Kα Emission

In addition to Kα emission excited by core radiation at peak compression, Kα radiation is also emitted during the laser-irradiation pulse. The latter emission can be seen in Fig. 75.27 (second image from the left) and in Fig. 75.29 as a weak ring of emission at a radius of ~300 μm. To better understand the origin of this emission, we simulate the transport through the target of radiation giving rise to Kα emission, both the primary (pumping) radiation and the secondary (or fluorescent) Kα radiation. We use profiles of target parameters calculated by the one-dimensional code *LILAC* to compute the transport of radiation of photon energy above the Ti *K*-edge, flowing radially outward and inward. The radiation is derived from the OPLIB astrophysical opacity tables[11] using the LTE approximation. To calculate the pumping of Kα fluorescence we must know the component of the total opacity (given by the tables) that is related to photoionization of *K*-shell electrons. At the *K* edge, this component is easily found from the *K*-edge jump in the opacity tables; for all higher photon energies we make use of its known dependence on photon energy. Finally, the Kα emission is transported along straight cords in the direction of observation, and the resulting profile is convolved with the instrumental broadening function (due to the pinhole's finite size).

Figure 75.30 compares the resulting Kα profile with the measured profile (from Fig. 75.29), normalized to the simulated profile. Two ring-shaped Kα emission zones are seen: an intense ring at a radius of ~80 μm and a weaker ring at a radius of ~300 μm. In the experiment (Fig. 75.27), only sections of each ring are observed (along the vertical axis) because the crystal limits the field of view in the direction of dispersion. The simulations show that the strong, inner ring is emitted around peak compression and is pumped by outgoing core radiation; on the other hand, the weak, outer ring is emitted during the laser-irradiation pulse and is pumped by ingoing coronal radiation. The nonuniformity in the measured image (higher intensity at positive radial distances) was discussed above. Figure 75.30 shows that the position of the cold shell during the laser pulse and during peak compression is in rough agreement with one-dimensional code predictions, in spite of the marked nonuniformity. It should be noted, however, that the inner, undoped shell is not detected by the Kα emission;

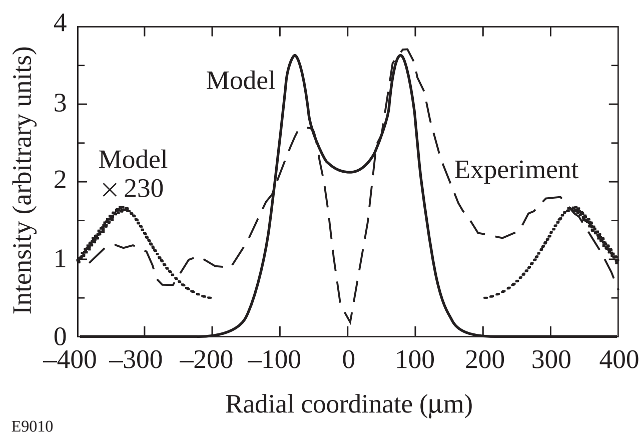

Figure 75.30
Measured and simulated radial profile of Kα emission for target shot (b). The inner ring of ~80-μm radius marks the position of the cold shell around the time of peak compression and is pumped by core radiation. The outer ring of ~300-μm radius marks the position of the shell during the laser pulse and is pumped by coronal radiation. The simulation includes only radiation transport, and the required multiplication by a factor of 230 shows that the outer ring is pumped by suprathermal electrons rather than by radiation.

the behavior of that segment of the shell is most indicative of target performance.

Whereas the position of the outer Kα emission ring is quite well predicted by the code, its intensity is not: we must multiply its calculated intensity by ~230 to match the experiment. The only obvious explanation is that the outer ring of Kα emission is mostly excited not by radiation but by suprathermal electrons, which are not included in the simulations. This question can be asked: How does the assumption of LTE in the radiation-transport calculations affect these conclusions? First, the LTE assumption affects mostly the intensity of the emission rings rather than their position. Second, departures from LTE would be more severe in the outer ring (of lower density) and would reduce the radiation available for pumping. Thus, the outer Kα ring would be even weaker with respect to the inner Kα ring than with the LTE calculations.

We now estimate the total preheat energy E_{ph} deposited in the target, based on the energy $E_{\mathrm{K}\alpha}$ of electron-excited Kα emission. The total Kα energy of the outer ring, measured by a spatially integrating spectrometer, is $E_{\mathrm{K}\alpha}$ ~10 mJ. For suprathermal-electron temperatures T_h above ~10 keV the ratio $R = E_{\mathrm{ph}}/E_{\mathrm{K}\alpha}$ tends to a constant independent of T_h. For medium-Z elements this constant is ~170;[12] thus, the preheat energy deposited in the titanium part of the shell is ~10 mJ × 170 = 1.7 J. To estimate the total preheat of the Ti-doped shell we note that the deposition rate for electrons in CH (over a very wide electron energy range) is ~10 times higher than that in Ti at 2% concentration;[13] thus, the preheat energy deposited in the doped shell is ~17 J. Since about half of the unablated shell is doped, this brings the total preheat energy to ~34 J. This estimate of preheat energy is independent of T_h; it only assumes that T_h is well above ~10 keV. The suprathermal electrons surmised from the Kα emission can give rise to fast (or suprathermal) ions. In fact, total fast-ion energies of the order of 10 J (and ion energies >> 10 keV) have been measured by the charged-particle spectrometer on similar OMEGA target shots; thus, the two measurements are consistent.

In conclusion, a simple imaging method for laser-fusion experiments has been demonstrated. Placing a multi-pinhole array in front of a flat-crystal spectrometer yields monochromatic, two-dimensional images with an ~100- to 150-μm field of view, sufficient for imaging cores of highly compressed targets. Images of the whole target are also obtained, with an ~100-eV bandwidth of the continuum. The method was applied to imaging the Kα fluorescence, shown to be excited by the core radiation at peak compression. This latter method yields the image of the cold shell at peak compression without using backlighting. Sufficient intensity has been shown to be obtained with 25-μm pinholes and a flat, nonfocusing diffracting crystal. Additionally, high spectral resolution was shown to be obtained with the array. This is particularly useful when measuring lines from the laser-interaction region, where the size of the target limits the spectral resolution to ~100, whereas with the array, the resolution can be five times higher. Finally, preheat in the amount of ~40 J was deduced from Kα emission during the laser pulse, which appears as an outer ring of ~300-μm radius.

ACKNOWLEDGMENT

This work was supported by the U.S. Department of Energy (DOE) Office of Inertial Confinement Fusion under Cooperative Agreement No. DE-FC03-92SF19460, the University of Rochester, and the New York State Energy Research and Development Authority. The support of DOE does not constitute an endorsement by DOE of the views expressed in this article.

REFERENCES

1. C. L. S. Lewis and J. McGlinchey, Opt. Commun. **53**, 179 (1985).
2. J.-C. Kieffer *et al*., Appl. Opt. **28**, 4333 (1989).
3. C. Brown *et al*., Rev. Sci. Instrum. **68**, 1099 (1997).
4. F. J. Marshall and J. A. Oertel, Rev. Sci. Instrum. **68**, 735 (1997).
5. M. Vollbrecht *et al*., J. Quant. Spectrosc. Radiat. Transf. **58**, 965 (1997).
6. H. Azechi *et al*., Appl. Phys. Lett. **37**, 998 (1980).
7. T. R. Boehly, R. S. Craxton, T. H. Hinterman, J. H. Kelly, T. J. Kessler, S. A. Kumpan, S. A. Letzring, R. L. McCrory, S. F. B. Morse, W. Seka, S. Skupsky, J. M. Soures, and C. P. Verdon, Rev. Sci. Instrum. **66**, 508 (1995).
8. B. Yaakobi, F. J. Marshall, D. K. Bradley, J. A. Delettrez, R. S. Craxton, and R. Epstein, Phys. Plasmas **4**, 3021 (1997).
9. B. Yaakobi and F. J. Marshall, J. Quant. Spectrosc. Radiat. Transfer **61**, in press.
10. D. J. Botto, J. McEnnan, and R. H. Pratt, Phys. Rev. A **18**, 580 (1978).
11. M. F. Argo and W. F. Huebner, J. Quant. Spectrosc. Radiat. Transfer **16**, 1091 (1976).
12. B. Yaakobi, J. Delettrez, L. M. Goldman, R. L. McCrory, W. Seka, and J. M. Soures, Opt. Commun. **41**, 355 (1982).
13. G. Knop and W. Paul, in *Alpha-, Beta- and Gamma-Ray Spectroscopy*, 1st ed., edited by K. Siegbahn (North-Holland, Amsterdam, 1965), Vol. 1, p. 12; L. V. Spencer, *Energy Dissipation by Fast Electrons*, National Bureau of Standards, Monograph 1 (U.S. Government Printing Office, Washington, DC, 1959).